Comparative analysis of nanoindentation-induced incipient deformation of zirconium-based bulk metallic glass in various structural states

Silvia Pomes[a,b], Nozomu Adachi[c], Masato Wakeda[b], Takahito Ohmura[a,b]

[a]*Department of Materials Science and Engineering, Graduate School of Engineering, Kyushu University, 774 Motooka, Nishi-ku, Fukuoka 819-0395, Japan*

[b]*Research Center for Structural materials, National Institute for Materials Science, 1-2-1 Sengen, Tsukuba 305-0047, Japan*

[c]*Department of Mechanical Engineering, Toyohashi University of Technology, 1-1 Hibarigaoka, Tempaku, Aichi, 441-8580, Japan*

E-mail addresses:

Silvia Pomes pomes.silvia@nims.go.jp

Nozomu Adachi adachi.nozomu.tq@tut.jp

Masato Wakeda wakeda.masato@nims.go.jp

Corresponding author: Takahito Ohmura ohmura.takahito@nims.go.jp

The incipient plastic deformation behaviour of as-cast and annealed samples of $Zr_{50}Cu_{40}Al_{10}$ (atom %) bulk metallic glass was investigated by nanoindentation. A validated load-over-displacement versus displacement plot showed the existence of a precursor event to incipient plasticity in both samples. The activation stress remained consistent in both samples, indicating that the event corresponds to local behaviour in regions with the same energy state, and it is not influenced by the overall microstructure. Conversely, the first serration detected in the as-relaxed sample exhibited a greater magnitude, potentially arising from a distinct energy-dissipation rate related to larger-scale microstructural characteristics.

Keywords: A. metallic glass, **B.** mechanical properties, **B.** inhomogeneous transformation, **D.** free volume, **F.** nanoindentation

1. Introduction

Instrumented nanoindentation testing is extensively used in the nanomechanical characterization of bulk metallic glasses (BMG) because of its ability to probe small volumes, enabling the study of local responses to applied loads, and the investigation of the underlying deformation processes [1,2]. Upon testing BMG, a close examination of the loading segment on the load–displacement (P–h) curve initially reveals the presence of an elastic deformation, in accordance with the Hertzian equation [3]. Subsequently, a distinctive serrated flow is observed [4–8]. Schuh and Nieh [9] demonstrated that these serrations correspond to the formation of shear bands. This finding was further supported by Mukhopadhyay et al. [10] and was confirmed by atomic-force microscopy. Indeed, deformation through shearing is a widely accepted concept in BMG and is regarded as a stress-activated process occurring among atoms susceptible to structural relaxation [11,12]. In the analysis of the loading segment, the P/h–h plot [13] is a state-of-the-art tool for the nanomechanical characterization of metallic materials [14] and it has proved essential in detecting the occurrence of precursor events to incipient plasticity in BMG [15].

Owing to the limitations of experimental research, numerical protocols have been proposed for quantitatively assessing the features of the underlying deformation mechanisms in BMG. From a theoretical perspective, serrated flow observed in BMG, considered a signature of the activation and propagation of a shear band[16], has been

connected to the overcoming of a specific potential energy barrier [17,18]. By considering the potential energy landscape theory [17], a universal criterion for plastic yielding at room temperature was formulated by Johnson and Samwer [18] as the cooperative shear model (CSM). On the basis of this model and nanoindentation data, Schuh and Lund [19] formulated a mathematical method to estimate the activation volume for the stress-assisted nucleation of defects, characterizing the incipient plastic flow in a crystalline material. The method was successfully applied by Choi et al. [20] to estimate the volume of the shear-transformation zone (STZ) in a BMG, by performing a statistical analysis of the maximum shear stress associated with the onset of the first serration. In our earlier investigation of a Zr-based BMG [15], which involved the use of nanoindentation *P/h–h* plots and a statistical analysis, we successfully detected a pre-serration deformation, corresponding to a deviation of the data from the Hertz curve for elastic contact. This phenomenon was identified as a thermally activated process, followed by a similarly thermally activated serration.

In the present study, we explored the influence of the bulk microstructure on the early stages of deformation by probing pre-serration processes and the first serration in a Zr-based metallic glass in various structural states, through nanoindentation.

By employing experimental, theoretical, and statistical analyses, this work unveils the potential physical mechanisms governing early-stage deformation and elucidates the influence of the bulk configuration on the incipient deformation dynamics.

2. Experimental

Two samples, as-cast and as-relaxed, of $Zr_{50}Cu_{40}Al_{10}$ (atom %) BMG were investigated. The alloy was produced by arc-melting and tilt-casting in the form of rods with a diameter of 10 mm [21,22]. The as-relaxed state was obtained from the as-cast rod by annealing for three hours at 659 K, which is 40° below the glass-transition temperature (T_g = 693 K). Each sample was sectioned into 2-mm-thick discs from the rod. Then, the disc samples were polished using sandpaper with a grit size of up to #4000 and diamond suspension with particle sizes up to 1 μm. A sol–gel Al_2O_3 suspension with a particle size of 0.05 μm was used to remove the damaged surface layer produced by the mechanical polishing. The final surface roughness (RMS) was 1 nm.

A Hysitron Triboindenter TI950 (Bruker Co., Minneapolis, MN, USA), equipped with a Berkovich indenter, was employed to perform nanoindentation testing in the load-control mode with a peak load of 300 μN, a loading rate of 10 μN/s, and an acquisition rate of 300 points/s. To prevent any interaction between induced strain fields, a spatial separation of 3 μm was maintained between the test locations. To ensure statistical significance, 130 tests were performed on each sample [23]. Nanoindentation tests were analyzed on a *P/h–h* plot, as described previously [15], and were complemented by statistical and numerical analyses [18–20].

3. Results and Discussion

Figure 1(a) shows typical *P–h* plots for the two samples: the curve corresponding to the as-relaxed sample has been shifted horizontally to facilitate visualization. The data obtained from the as-cast and as-relaxed samples are shown in yellow and blue, respectively; this colour coding is used consistently throughout this report. A typical image of an indentation mark, obtained by using an atomic-force microscope embedded in the nanoindentation machine, is shown in the inset of Figure 1(a). As estimated by using the Oliver–Pharr method [24], the as-cast and as-relaxed samples exhibited an average hardness H of 4.21 ± 0.36 GPa and 4.39 ± 0.30 GPa, respectively, and reduced moduli E_r of 86.5 ± 5.6 GPa and 92.8 ± 5.3 GPa, respectively. Serrations were slightly observable in both loading segments; hence, to detect them more clearly, the loading segments were replotted in the form of a *P/h–h* graph in Figure 1(b). Notably, the as-relaxed curve has been shifted vertically for easier visualization.

As in our previous study [15], the characteristic deformation parameters are defined as follows: *point HZ* represents the deviation of the experimental data from the Hertz curve corresponding to an initiation of inelastic behaviour, whereas *point A* and *point B* indicate the onset and completion of a serration event, respectively, and the *AB event size* is the horizontal distance in displacement between *point A* and *point B*.

The main plots in Figure 2(a) show the load (P_{HZ}) and displacement values corresponding to *point HZ*, whereas the side histograms show the probability distribution of each variable on the axis. The Hertz curves for the two samples are indicated by red lines and were calculated by using the following equation

112 $$P = \frac{4}{3} E_r \sqrt{R h^3}, \qquad (1$$

113 fitting parameter E_r with a fixed indenter tip radius R equal to 700 nm. Because every
114 point lies on the curve, this confirms that *point HZ* represents the initial point of
115 plasticity as a pre-serration deformation [20]. The fitted E_r values for the as-cast and as-
116 relaxed samples were 83.6 GPa and 89.7 GPa, respectively, which were almost identical
117 to the values obtained independently by the unloading analysis. The side histograms
118 show a Gaussian-like distribution and an almost identical average and deviation in both
119 samples.

120 Figure 2(b) is a plot for *point A*, akin to Figure 2(a). The primary plot reveals a positive
121 correlation between higher P values and a greater h, echoing the pattern observed in the
122 *point HZ* distribution of Figure 2(a). However, compared with Figure 2(a), the data
123 exhibit an increased dispersion. This variance might stem from the stochastic nature of
124 plasticity following *point HZ*. The side histograms in Figure 2(b) display a distribution
125 of P that is reminiscent of a Gaussian-like curve, similar to that featured in Figure 2(a).
126 Furthermore, they show a remarkable difference in the average value that is higher for
127 the as-relaxed sample.

128 Figure 2(c) illustrates the distribution plot of P at *point A* (P_A) relative to the magnitude
129 of the *AB event*. In this representation, the data points exhibit a scattered pattern devoid
130 of any discernible trend. This observation implies that the size of the *AB event* size is
131 independent of P_A. The accompanying histograms for the *AB event* size do not exhibit a
132 distinct Gaussian profile. These outcomes collectively suggest a distinct physical basis
133 for *points HZ* and *A* in comparison to the *AB event* in both samples.

To identify the underlying nature of these phenomena, complementary cumulative distribution functions (CCDF) for P_{HZ} and P_A are presented in Figs. 3(a) and 3(b), respectively. Figure 3(c) shows the CCDF for the *AB event* size: due to the limited data range (0.6–2.5 nm), a further analysis of the distribution would not have been significant and was, therefore, not performed. Across Figures 3(a) and 3(b), all the data points show a Gaussian-like distribution. This alignment reinforces the findings described in Figures 2(a) and 2(b), supporting the notion that these events potentially stem from thermally activated processes. This observation concurs with the work of Tönnies et al. [25], who reported that the triggering dynamics of the first serration are influenced by thermal fluctuations.

We therefore evaluated the activation volumes involved in the deformation processes at *point HZ* and *point A* by applying the stress-biased thermal activation model for indentation-induced deformation [19,20]. The maximum shear stress (τ) underneath the indenter was estimated by means of the Hertz contact theory [3] as follows:

$$\tau = 0.18\left(\frac{E_r}{R}\right)^{\frac{2}{3}} \mathrm{P}_c^{\frac{2}{3}} \qquad (2$$

where P_c denotes P_{HZ} or P_A. The cumulative distribution of events *f* with respect to the maximum shear stress values is given as follows [19]:

$$f = 1 - \exp\left[-\frac{kT\dot{\gamma}_0}{v^*(d\tau/dt)}\exp\left(-\frac{\Delta F^*}{kT}\right)\exp\left(\frac{\tau v^*}{kT}\right)\right], \qquad (3$$

where v^* is the activation volume, kT is the thermal energy, $\dot{\gamma}_0$ is the attempt frequency and ΔF^* is the Helmholtz activation energy. The Helmholtz activation energy is the energy barrier for nucleation in the absence of external stimuli. In our experimental

setting, the stress rate is almost constant because the loading rate is constant. The plot is displayed in Figure 4(a), in which the results for *point HZ* and *point A* are plotted as triangular and circular markers, respectively.

To estimate the activation volume, Eq. (2) is rewritten as,

$$\ln[\ln(1-f)^{-1}] = \left\{\frac{\Delta F^*}{kT} + \ln\left[\frac{kT}{v^*(d\tau/dt)}\right]\right\} + \frac{v^*}{kT}\tau. \quad (4$$

By excluding the tails of distributions, the data in Figure 4(a) are replotted in Figure 4(b) according to Eq. (4). The activation volumes for the events at *points HZ* and *A* are determined from the slopes of the plots by linear regression fitting. The slope values are displayed in Figure 4(b) and the calculated values of v^* are listed in Table 1.

Based on the CSM, the explicit formulation of the volume of the STZ (Ω) with respect to the activation volume is given as [20]:

$$\Omega = \frac{\tau_0}{6C\xi G_0 {\gamma_c}^2\left(1-\frac{\tau}{\tau_0}\right)^{\frac{1}{2}}} v^*, \quad (5$$

where C and ξ are constants equal to 1/4 and 3, respectively; $G_0 = E_r/2(1+\nu)$ is the shear modulus at $T = 0\ K$; τ and τ_0 are the threshold shear strengths at temperatures T and 0 K, respectively; and $\gamma_c = \tau/G$ is the critical shear strain at yielding. Previous studies have demonstrated that the shear modulus does not affect the estimation of the STZ volume to any major extent, and that it exhibits a weak temperature dependence [20,26]. By integrating Poisson's ratio (ν) as 0.36 for both samples [27], the G_0 values obtained for the as-cast and as-relaxed samples are 32 and 34.2 GPa, respectively.

Parameters γ_c, τ, and τ_0 are calculated using the scaling law proposed by Johnson and Samwer [18]. The values obtained for Ω are listed in Table 1.

An approximation of the number of atoms (*N*) involved in the STZ is obtained by considering the microstructure of the sample as a random arrangement of densely packed hard spheres with an average atomic radius (r_{avg}) given by

$$r_{avg} \approx \left(\sum_i^n A_i {r_i}^3\right)^{\frac{1}{3}}, \qquad (6$$

where A_i and r_i are the atomic fraction and atomic radius, respectively, of each alloying element. The calculated average atomic radius is 0.137 nm, considering the values for the covalent atomic radius reported in the literature [28]. The values of *N* are listed in Table 1. The calculated values of v^*, Ω and *N* are consistent, in terms of their order of magnitude, with results reported in previous studies on Zr-based BMG [20,22,26,27,29].

Table 1. Estimated values of the activation volume v^*, the STZ volume Ω, and the number of atoms in STZ *N* at the points *HZ* and *A* in as-cast and as-relaxed samples

	As-cast		As-relaxed	
	HZ	*A*	*HZ*	*A*
v^* $[nm^3]$	0.023	0.030	0.022	0.039

Ω $[nm^3]$	0.517	0.662	0.486	0.859
N [atom]	48	61	45	79

188

189 The as-cast and as-relaxed samples showed different behaviours. The average value of
190 P_A is higher for the as-relaxed sample than for the as-cast sample, as shown in Figures
191 2(b) and 3(b). In addition, the size of the *AB event* shifts to a higher range in the
192 distribution, as shown in Figure 3(c). This behaviour is presumably due to the
193 differences in the atomic configuration.

194 Prior to deformation, the as-relaxed sample is presumed to display a denser
195 microstructure, characterized by a reduced volume fraction of unstable regions, owing
196 to the energy input during the annealing treatment, resulting in the formation of stronger
197 bonds. Experimental evidence for the increase in the atomic-packing density after sub-
198 T_g annealing has been provided by Pan et al. [30] and confirmed by X-ray diffraction
199 analyses of $Zr_{50}Cu_{40}Al_{10}$ (atom %) BMG as-cast and annealed samples [31].

200 At *point HZ*, the same values are found for both the critical load P_{HZ} and the activation
201 volume in the as-cast and as-relaxed samples. This suggests that the atomic
202 rearrangement at *point HZ* of pre-serration deformation might correspond to a highly
203 localized process occurring in the unstable region. Furthermore, given that both samples
204 are composed of the same alloying elements, the enthalpy of formation associated with
205 the weakest interatomic bond is identical in both samples, as is the potential energy

206 barrier associated with their configuration [17]. The absence of differences in *point HZ*
207 events, both in their physical nature and scale, suggests that the different degrees of
208 microstructural heterogeneity of the bulk samples do not affect the incipient
209 deformation mechanics.

210 At *point A*, the critical load P_A of the as-cast sample is lower than that of the as-relaxed
211 sample. Choi et al. [29] and Tao et al. [31] reported that as-cast Zr-based BMG samples,
212 as well as the sub-T_g annealed samples, exhibited a similar occurrence of smaller critical
213 loads and STZ sizes at the first pop-in. Tao et al. recently confirmed their findings by
214 using nanoindentation creep and strain-rate sensitivity methods [32,33]. In this work,
215 and in line with previous studies, the aforementioned occurrence is explained in terms
216 of the different structural configurations of the samples. In the as-cast sample, the
217 volume fraction of easily movable atoms is higher; consequently, these atoms are nearer
218 to one another, and a smaller applied stress is required to trigger the cooperative
219 shearing phenomenon. From an energetic standpoint, the as-cast microstructure is more
220 unstable overall; consequently, the energy quota required to reach the serration energy
221 barrier is smaller.

222 Regarding the size of the *AB event*, longer serrations detected in the as-relaxed sample
223 might be due to the larger distance to which the strain is accommodated in the more-
224 uniform microstructure and to the slower energy-dissipation rate over smoother
225 potential-energy landscape transition states.

226

4. Conclusion

In brief, we have conducted a comparative analysis of the early stages of deformation in as-cast and as-relaxed $Zr_{50}Cu_{40}Al_{10}$ (atom %) BMG by nanoindentation testing. Any unstable deformation mode during loading was clearly visualized using a *P/h–h* plot. The work yielded the following findings.

(1) The critical stress value at *point HZ,* corresponding to the pre-serration event, was consistent between the two samples, indicating that the event represents a local behaviour occurring in regions characterized by the same energy state and that it is not subject to the influence of the overall microstructure.

(2) The critical load at *point A* of the as-cast sample is lower than that of the as-relaxed sample. This difference could be attributed to the higher volume fraction of unstable regions in the as-cast sample, so that a smaller applied stress is required to trigger the serration.

(3) The magnitude of the *AB event* detected in the as-relaxed sample was greater than that in the as-cast sample, potentially due to a distinct energy-dissipation rate related to microstructural characteristics on a larger scale.

Acknowledgements: S.P. is grateful to acknowledge experimental support by Eri Nakagawa.

CRediT authorship contribution statement

Silvia Pomes: Conceptualization; Data curation; Formal analysis; Investigation; Methodology; Writing - original draft; Writing - review & editing. **Nozomu Adachi**: Funding acquisition; Resources; Writing - review & editing. **Masato Wakeda**: Writing - review & editing. **Takahito Ohmura**: Conceptualization; Funding acquisition; Methodology; Project administration; Resources; Supervision; Writing - review & editing.

Declaration of competing interest

The authors declare that they have no known competing financial interests or personal relationships that could have appeared to influence the work reported in this paper.

Data availability

Data are not available for public access.

Funding: This research did not receive any specific grant from funding agencies in the public, commercial, or not-for-profit sectors.

References

[1] Zhang M, Chen Y, Li W. On the origin of softening in the plastic deformation of metallic glasses. Int. J. Plast. 2019;116:24–38:. doi: 10.1016/j.ijplas.2018.12.004.

[2] Zhang L, Ohmura T. Plasticity initiation and evolution during nanoindentation of an iron–3% silicon crystal. Phys. Rev. Lett. 2014;112:145504. doi: 10.1103/PhysRevLett.112.145504.

[3] Johnson KL. One hundred years of Hertz contact. Proc. Inst. Mech. Eng. 1982;196(1):363–378. doi: 10.1243/pime_proc_1982_196_039_02.

[4] Argon AS. Plastic deformation in metallic glasses. Acta Metall. 1979;27(1):47–58. doi: 10.1016/0001-6160(79)90055-5.

[5] Kimura H, Masumoto T. A model of the mechanics of serrated flow in an amorphous alloy. Acta Metall. 1983;31(2):231–240. doi: 10.1016/0001-6160(83)90100-1.

[6] Pampillo CA, Chen HS. Comprehensive plastic deformation of a bulk metallic glass. Mater. Sci. Eng. 1974;13(2):181–188. doi: 10.1016/0025-5416(74)90185-2.

[7] Spaepen F. A microscopic mechanism for steady state inhomogeneous flow in metallic glasses. Acta Metall. 1977;25: doi: 10.1016/0001-6160(77)90232-2.

[8] Maaß R. Beyond serrated flow in bulk metallic glasses: what comes next? Metall. Mater. Trans. A. 2020;51:5597–5605. doi: 10.1007/s11661-020-05985-w.

[9] Schuh CA, Nieh TG. A nanoindentation study of serrated flow in bulk metallic glasses. Acta Mater. 2003;51(1):87–99. doi: 10.1016/S1359-6454(02)00303-8.

[10] Mukhopadhyay NK, Belger A, Paufler P, et al. Nanoindentation studies on Cu–Ti–Zr–Ni–Si–Sn bulk metallic glasses. Mater. Sci. Eng. A. 2007;449–551:954–957. doi: 10.1016/j.msea.2006.02.258.

[11] Argon AS. Plastic deformation in metallic glasses. Acta Metall. 1979;27(1):47–58. doi: 10.1016/0001-6160(79)90055-5.

[12] Argon AS. Strain avalanches in plasticity. Philos. Mag. 2013;93(28–30):3795–3808. doi: 10.1080/14786435.2013.798049.

[13] Sekido K, Ohmura T, Sawaguchi T, et al. Nanoindentation/atomic force microscopy analyses of e-martensitic transformation and shape memory effect in Fe–28Mn–6Si–5Cr alloy. Scr. Mater. 2011;65(11):942–945. doi: 10.1016/j.scriptamat.2011.08.010.

[14] Ohmura T. Nanomechanical characterization of metallic materials. In: Tanaka I, Tsuji N, Inui H, editors. The plaston concept: Plastic deformation in structural materials. Singapore: Springer Nature Singapore; 2022. p. 157–195. doi: 10.1007/978-981-16-7715-1_8.

[15] Pomes S, Adachi N, Wakeda M, Ohmura T. Probing pre-serration deformation in Zr-based bulk metallic glass via nanoindentation testing. Scr. Mater. 2023;237:115713. doi: 10.1016/j.scriptamat.2023.115713.

[16] Maaß R, Klaumünzer D, Löffler JF. Propagation dynamics of individual shear bands during inhomogeneous flow in a Zr-based bulk metallic glass. Acta Mater. 2011;59(8):3205–3213. doi: 10.1016/j.actamat.2011.01.060.

[17] Wales DJ. A microscopic basis for the global appearance of energy landscapes. Science. 2001;293(5537):2067–2070. doi: 10.1126/science.1062565.

[18] Johnson WL, Samwer K. A universal criterion for plastic yielding of metallic glasses with a $(T/T_g)^{2/3}$ temperature dependence. Phys. Rev. Lett. 2005;95:199501. doi: 10.1103/PhysRevLett.95.195501.

[19] Schuh CA, Lund AC. Application of nucleation theory to the rate dependence of incipient plasticity during nanoindentation. J. Mater. Res. 2004;19: 2152–2158. doi: 10.1557/JMChoi R2004.0276.

[20] Choi I-C, Zhao Y, Yoo B-G, et al. Estimation of the shear transformation zone size in a bulk metallic glass through statistical analysis of the first pop-in stresses during spherical nanoindentation. Scr. Mater. 2012;66(11):923–926. doi: 10.1016/j.scriptamat.2012.02.032.

[21] Yokoyama Y, Fredriksson H, Yasuda H, et al. Glassy solidification criterion of $Zr_{50}Cu_{40}Al_{10}$ alloy. Mater. Trans. 2007;48(6):1363–1372. doi: 10.2320/matertrans.MF200624.

[22] Adachi N, Todaka Y, Ohmura T. Macroscopic viscoelastic deformation at room temperature in mechanically rejuvenated Zr-based metallic glass. MRS Commun. 2021;11:330–335. doi: 10.1557/s43579-021-00023-1.

[23] Nag S, Narayan RL, Mukhopadhyay Jang J-I, et al. Statistical nature of the incipient plasticity in amorphous alloys. Scr. Mater. 2020;187:360–365. doi: 10.1016/j.scriptamat.2020.06.045.

[24] Oliver WC, Pharr GM. An improved technique for determining hardness and elastic modulus using load and displacement sensing indentation experiments. J. Mater. Res. 1992;7:1564–1583. doi: 10.1557/jmr.1992.1564.

[25] Tönnies D, Samwer K, Derlet PM, et al. Rate-dependent shear-band initiation in a metallic glass. Appl. Phys. Lett. 2015;106:171907. doi: 10.1063/1.4919134.

[26] Limbach R, Kosiba K, Pauly S, et al. Serrated flow of CuZr-based bulk metallic glasses probed by nanoindentation: Role of the activation barrier, size and distribution of shear transformation zones. J. Non. Cryst. Solids. 2017;459: 130–141. doi: 10.1016/j.jnoncrysol.2017.01.015.

[27] Ma Y, Peng GJ, Debela TT, et al., Nanoindentation study on the characteristic of shear transformation zone volume in metallic glassy films. Scr. Mater. 2015;108:52–55. doi: 10.1016/j.scriptamat.2015.05.043.

[28] Pyykkö P, Atsumi M, Molecular single-bond covalent radii for elements 1–118. Chem. Eur. J. 2008;15(1):186–197. doi: 10.1002/chem.200800987.

[29] Choi IC, Zhao Y, Kim YJ, et al., Indentation size effect and shear transformation zone size in a bulk metallic glass in two different structural states. Acta Mater. 2012;60(19):6862–6868. doi: 10.1016/j.actamat.2012.08.061.

[30] Pan D, Yokoyama Y, Fujita T, et al. Correlation between structural relaxation and shear transformation zone volume of a bulk metallic glass. Appl. Phys. Lett. 2009;95:141909. doi: 10.1063/1.3246151.

[31] Tao K, Qiao JC, He QF, et al. Revealing the structural heterogeneity of metallic glass: Mechanical spectroscopy and nanoindentation experiments. Int. J. Mech. Sci. 2021;201:106469. doi: 10.1016/j.ijmecsci.2021.106469.

[32] Pan D, Inoue A, Sakurai T, et al. Experimental characterization of shear transformation zones for plastic flow of bulk metallic glasses. Proc. Natl. Acad. Sci. U. S. A. 2008;105(39): 14769–14772. doi: 10.1073/pnas.0806051105.

[33] Tao K, Khonik VA, Qiao JC. Indentation creep dynamics in metallic glasses under different structural states. Int. J. Mech. Sci. 2023;240:107941. doi: 10.1016/j.ijmecsci.2022.107941.

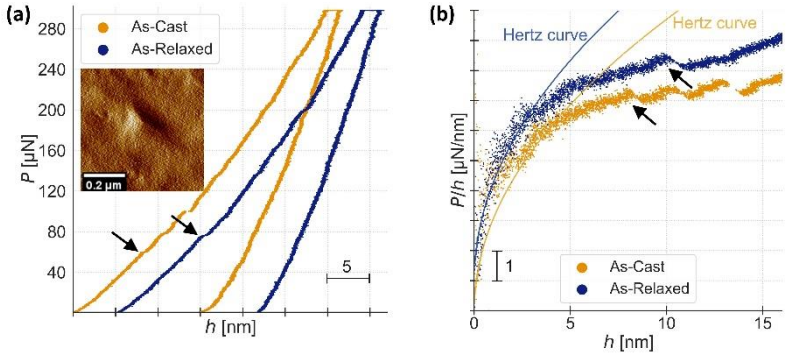

362

363 **Figure 1** (a) Representative load–displacement *P*–*h* curve for the $Zr_{50}Cu_{40}Al_{10}$ bulk
364 metallic glass as-cast (yellow) and as-relaxed (blue) samples. Serration is indicated by
365 black arrows. A resulting indentation mark is shown in the inset. (b) *P*/*h*–*h* curves
366 obtained from Figure 1(a): serrations exhibit a negative slope.

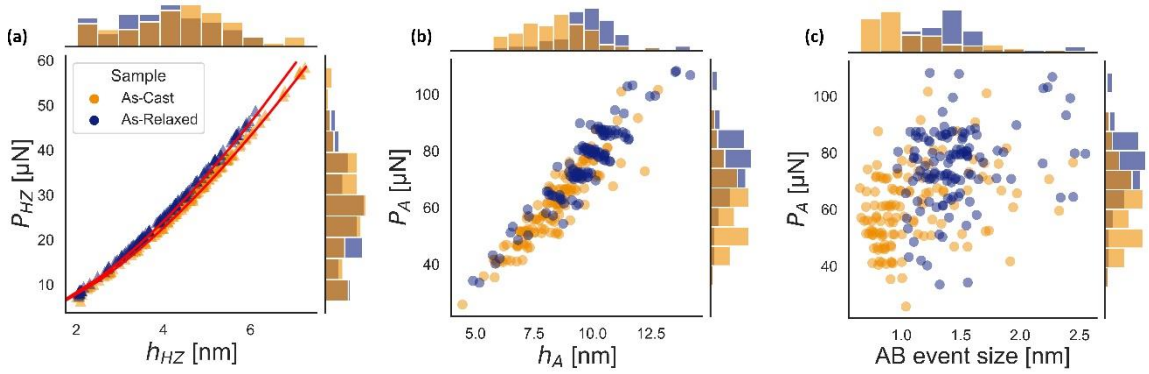

367

368 **Figure 2** Distribution plots for as-cast (yellow) and as-relaxed (blue) samples. (a)
369 Distribution of depth versus load at *point HZ*. Side histogram plots show probability
370 distributions. Hertz curves are displayed in red. (b) Distribution of depth versus load at
371 *point A*. (c) Distribution of the size at *event AB* versus the load at *point A*: the serration
372 size is not related to the activation load.

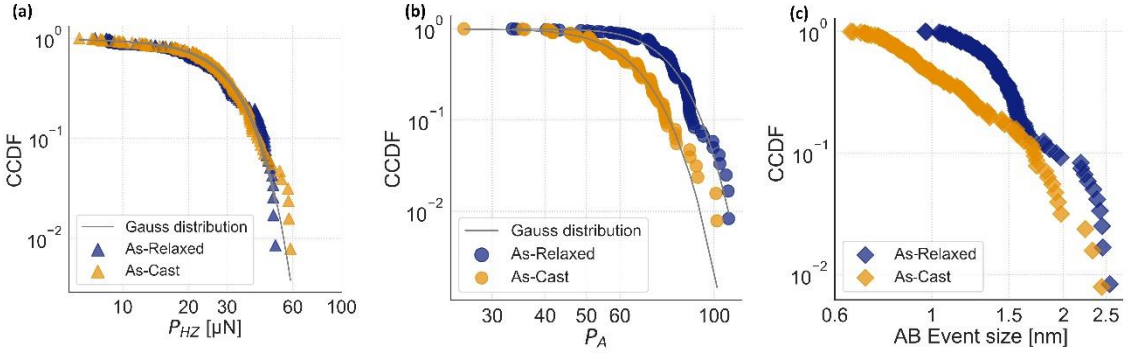

373

374 **Figure 3** Log–log plots of complementary cumulative distribution functions for as-cast
375 (yellow) and as-relaxed (blue) samples at (a) *point HZ*, (b) *point A* and (c) *AB event*
376 size.

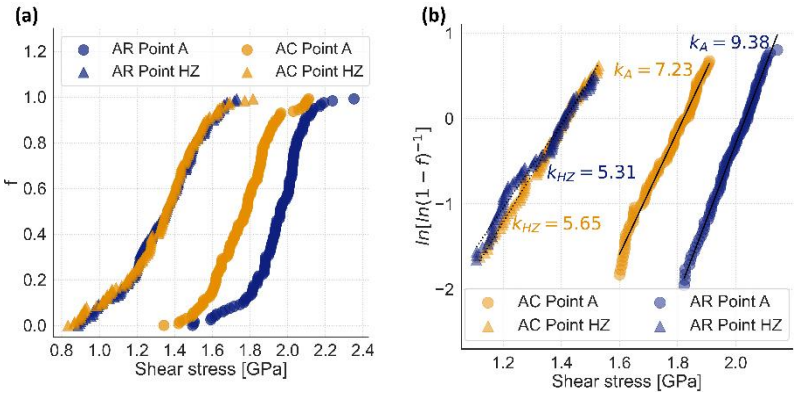

377

378 **Figure 4** (a) Cumulative distribution of maximum shear stress underneath the indenter
379 at *point HZ* (triangular marker) and *point A* (circular marker) for as-cast (AC; yellow)
380 and as-relaxed (AR; blue) samples. (b) Activation volume estimation at *points HZ* and
381 *A*.